Supporting Information

A salt-resistant Janus evaporator assembled from ultralong hydroxyapatite nanowires and nickel oxide for efficient and recyclable solar desalination

Dong-Dong Qin[a,b], Ying-Jie Zhu*[a,b], Ri-Long Yang[a,b], and Zhi-Chao Xiong*[a]

[a] State Key Laboratory of High Performance Ceramics and Superfine Microstructure, Shanghai Institute of Ceramics, Chinese Academy of Sciences, Shanghai, 200050, China

[b] Center of Materials Science and Optoelectronics Engineering, University of Chinese Academy of Sciences, Beijing 100049, China

* Corresponding author.

E-mail: y.j.zhu@mail.sic.ac.cn

zcxiong@mail.sic.ac.cn.

Heat loss analysis

The heat loss of the Janus water evaporator is mainly composed of three parts: (1) radiation; (2) convection; (3) conduction. The details of the analysis are displayed as followed.

(1) Radiation

The heat loss due to radiation is calculated using the Stefan-Boltzmann equation:

$$\Phi = \varepsilon\sigma\left(T_1^4 - T_2^4\right) \qquad (S1)$$

Where Φ is the radiation heat flux, ε is the emissivity (it is assumed that the absorber has a maximum emissivity of 1), σ is the Stefan-Boltzmann constant (5.67×10^{-8} W m^{-2} K^{-4}). T_1 is the surface temperature (≈ 44.5 °C) of the absorber under steady-state conditions, and T_2 is the ambient temperature (≈ 35.0 °C) of the absorber under 1 kW m^{-2} solar light irradiation.

Then, the radiation heat loss can be calculated based on the equation:

$$\eta_{rad} = \frac{\Phi}{Q_{in}} \qquad (S2)$$

Q_{in} is the input light irradiation flux to the surface of the photothermal paper. Under 1 kW m^{-2} solar light irradiation, the calculated radiation heat loss is 6.6 %.

(2) Convection

The heat loss of convection can be calculated by the following Newton's law:

$$Q_{conv} = hA(T_1 - T_2) \qquad (S3)$$

Where Q_{conv} is the heat energy, h and A represent the convection heat transfer coefficient (5 W m^{-2} K^{-1}) and surface area of the evaporator, respectively.

Then, the convection heat loss is calculated by the following equation:

$$\eta_{conv} = \frac{Q_{conv}}{AQ_{in}} = \frac{h(T_1 - T_2)}{Q_{in}} \qquad (S4)$$

Q_{in} is the input light irradiation flux to the surface of the photothermal paper. Under 1 kW m^{-2} solar light irradiation, the convection heat loss is 4.8 %.

(3) Conduction

The heat loss due to conduction can be calculated based on the following equation:

$$Q_{cond} = CmΔT \qquad (S5)$$

Where Q_{cond} is the heat flux, C is the specific heat capacity of water (4.2 kJ $^{o}C^{-1}$ kg^{-1}). In this work, m is the water weight (50 g), and ΔT is the average increased bulk water temperature (≈0.4 ^{o}C) under 1 kW m^{-2} solar light irradiation for 1 h. The conduction heat loss is calculated to be 1.9 %.

Based on the above analysis, the total heat loss of the hydrophilic HN/NiO photothermal paper is 13.3 % under 1 kW m^{-2} solar light irradiation. The light absorption of the hydrophilic HN/NiO photothermal paper is 92.1 %. The water evaporation efficiency should be lower than 78.8 %. According to the reference,[S1] the high actual water evaporation efficiency may be attributed to the high surface area of the evaporator.

Cai et. al. prepared the solar absorber TiO_2-PDA/PPy/cotton with a high surface area for solar desalination. The evaporation efficiency of the absorber is 98 % and the total heat loss including radiation, conduction and convection is about 28.54 %.[S1] In addition, Zhu et. al.[S2], Jiang et. al.[S3] and Wang et.al.[S4] reported the nearly ideal evaporation efficiencies of 100 % or over 100 % by increasing the actual surface area within a given projection area. According to the formula (1) in the main text, the evaporation efficiency is inversely proportional to the surface area of the absorber. On the one hand, the HN paper shows a porous network structure due to the interweaved ultralong hydroxyapatite nanowires (Fig. S2, ESI†). On the other hand, the hydrophilic HN/NiO photothermal paper displays a high surface area due to NiO nanoparticles (Fig. 1d and e). Hence, the actual surface area is much larger than the projected surface area which is adopted in the calculation of water evaporation rate and evaporation efficiency.

Furthermore, Yu et. al.[S5] reported that water molecules are more likely to evaporate as small clusters rather than individual molecules in a confined situation. Therefore, the vaporization enthalpy for a confined evaporation is smaller than the conventional latent heat

of bulk water which is adopted in the calculation of water evaporation efficiency. Although further study is needed, we presume that the confined water evaporation can take place from the photothermal layer of the evaporator. This may be another reason for the high actual water evaporation efficiency.

Fig. S1. Digital images of the commercial paper-making devices for the preparation of the large-sized HN/NiO photothermal paper. (a) The paper sheet former. (b) The paper presser. (c) The paper dryer.

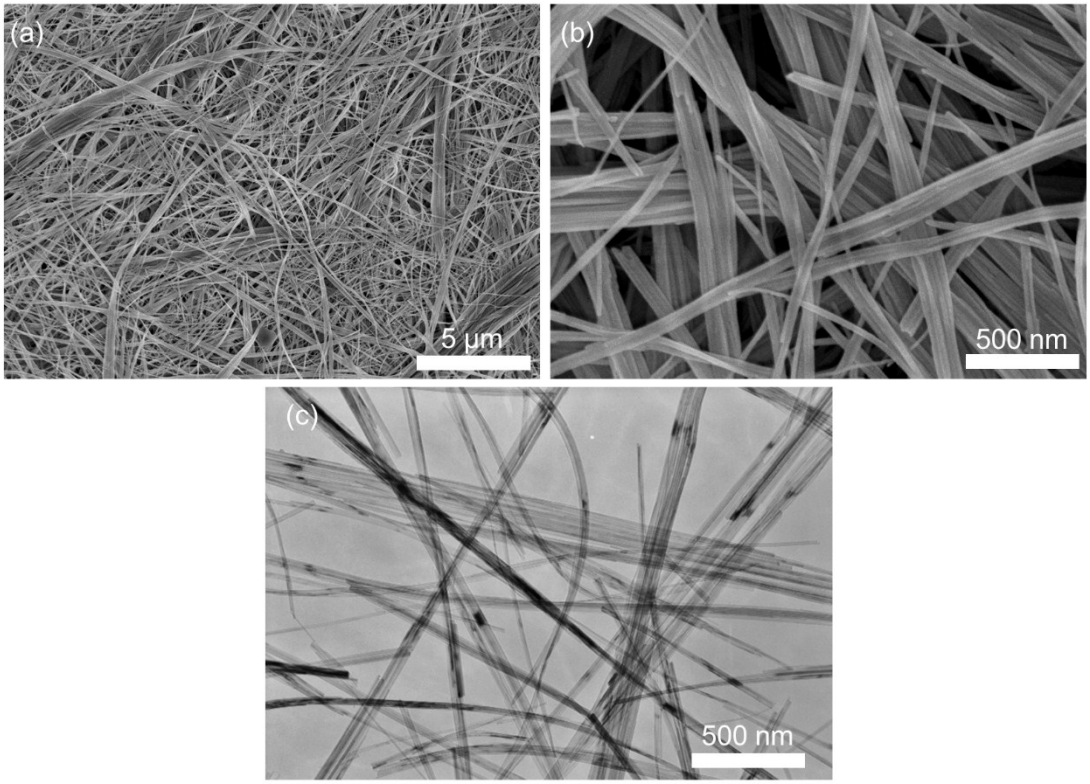

Fig. S2. SEM images (a, b) and TEM image (c) of the as-prepared ultralong hydroxyapatite nanowires (HNs).

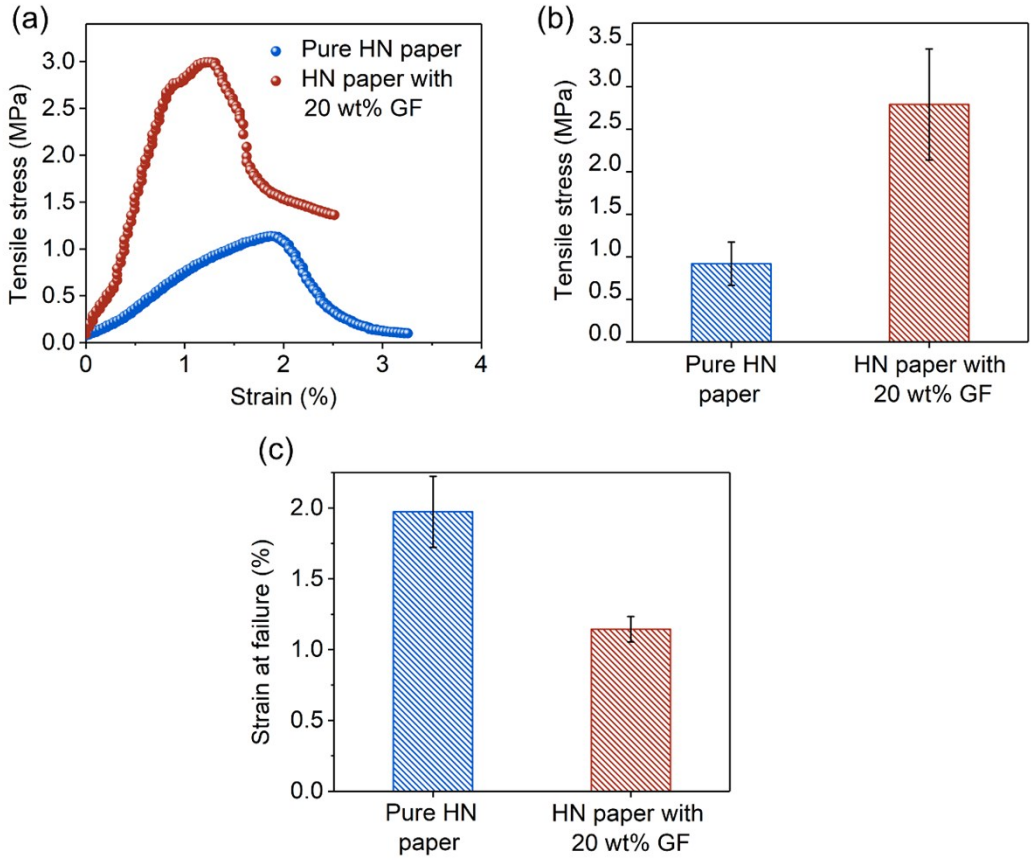

Fig. S3. Mechanical properties of the pure HN paper made from ultralong hydroxyapatite nanowires, and the HN paper made from 80 wt.% ultralong hydroxyapatite nanowires and 20 wt.% glass fibers (GFs). (a) Typical tensile stress-strain curves. (b) Ultimate tensile strength. (c) Strain at failure.

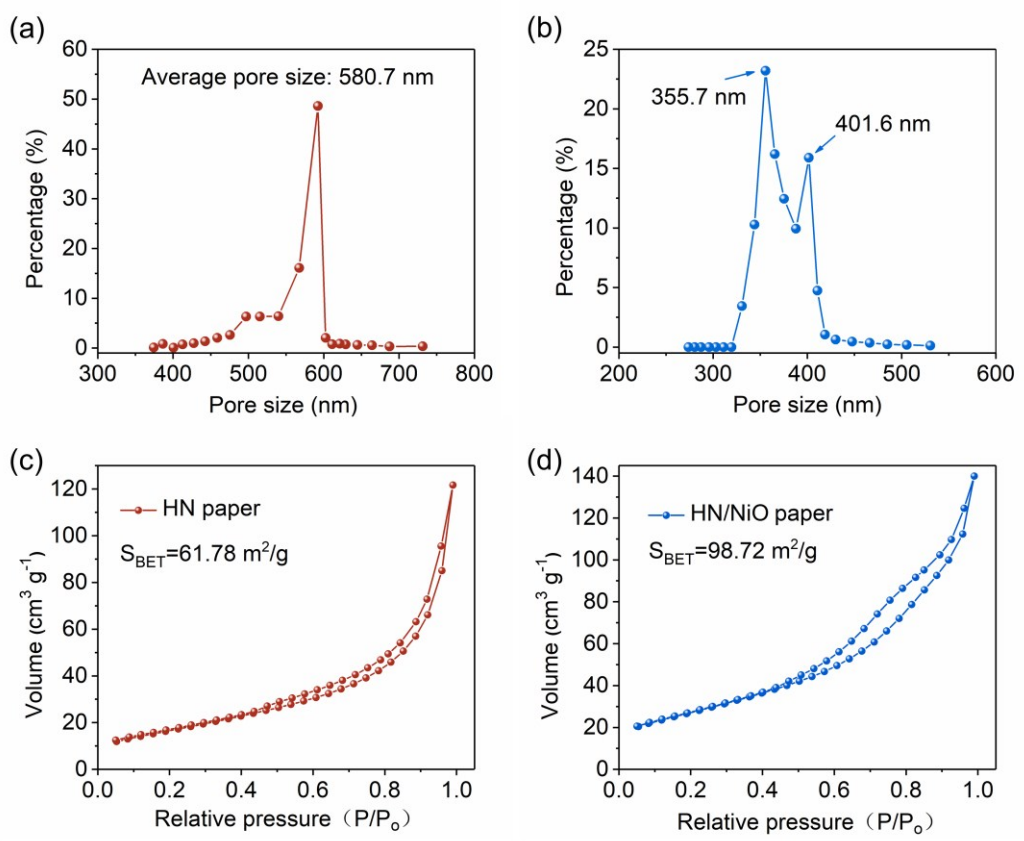

Fig. S4. (a, b) Pore size distribution curves measured using a pore size analyzer: (a) the HN paper; (b) the hydrophilic HN/NiO photothermal paper. (c, d) Nitrogen adsorption-desorption isotherm curves: (c) the HN paper; (d) the hydrophilic HN/NiO photothermal paper.

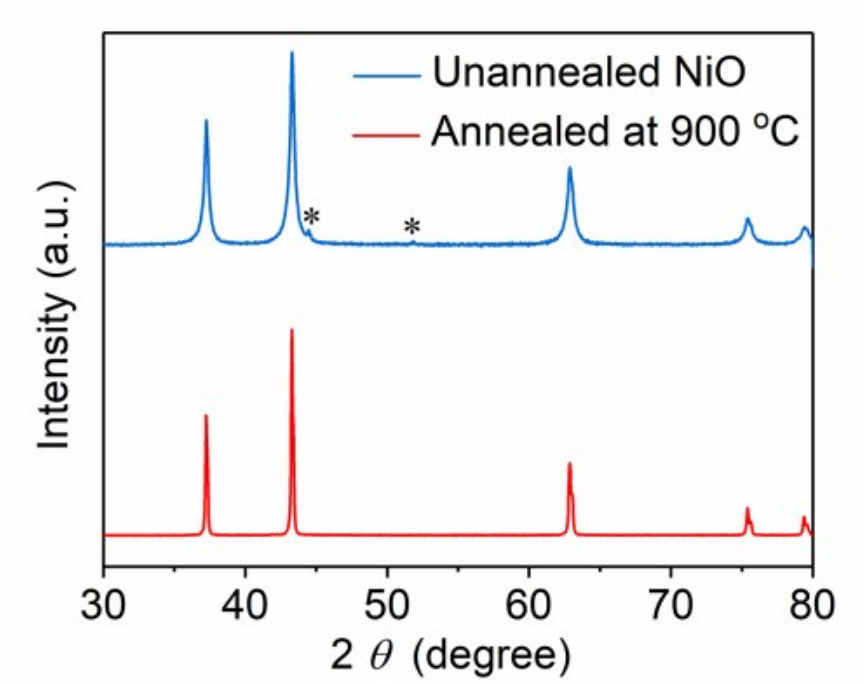

Fig. S5. XRD patterns of NiO nanoparticles before and after thermal treatment at 900 °C for 1 h in air atmosphere. The diffraction peaks of metallic Ni are labelled with a asterisk (∗).

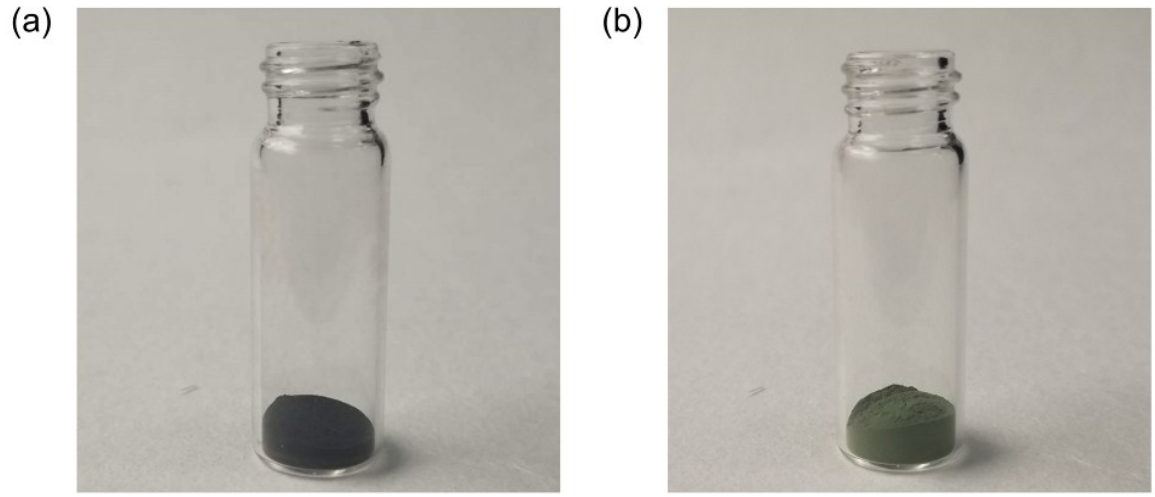

Fig. S6. Digital images of NiO powder before (a) and after (b) thermal treatment at 900 ^{o}C for 1 h in air atmosphere.

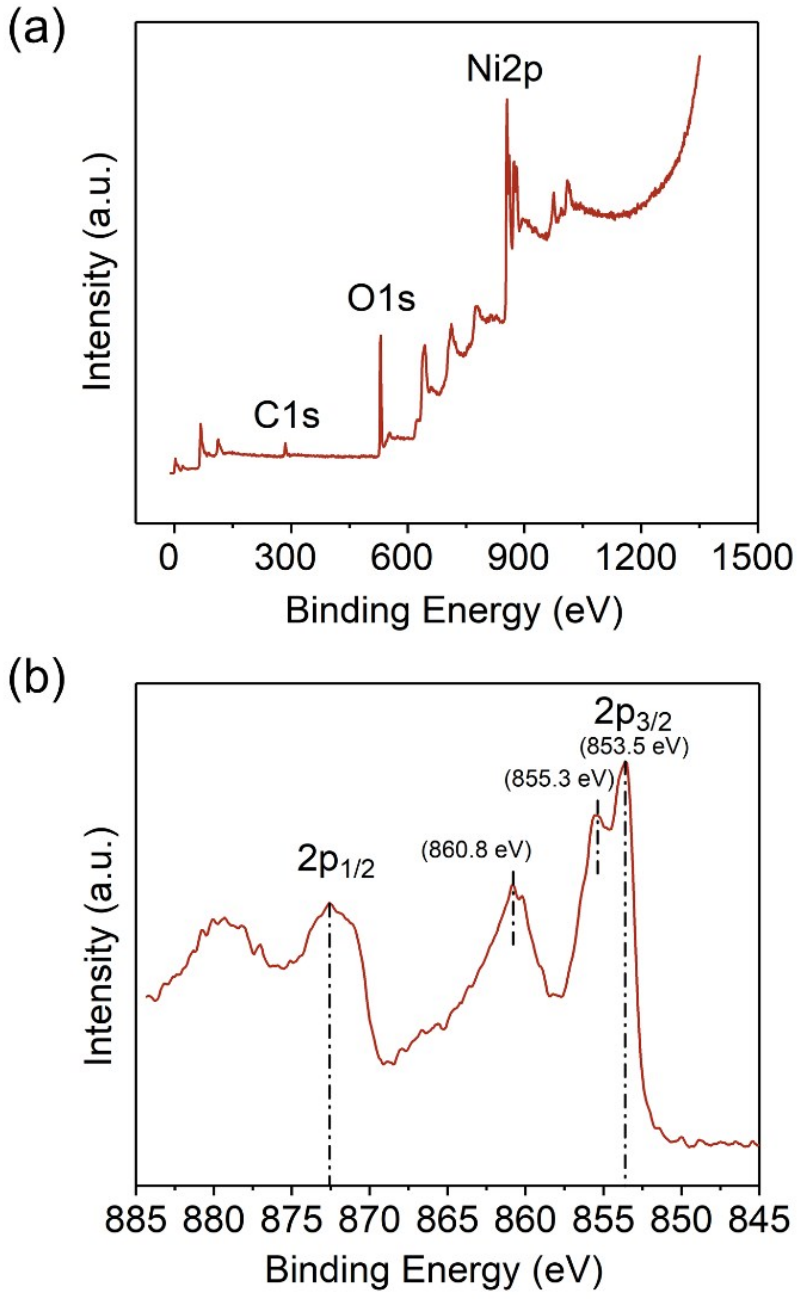

Fig. S7. XPS spectrum of black NiO nanoparticles: (a) a survey spectrum, and (b) the high-resolution spectrum of Ni 2p.

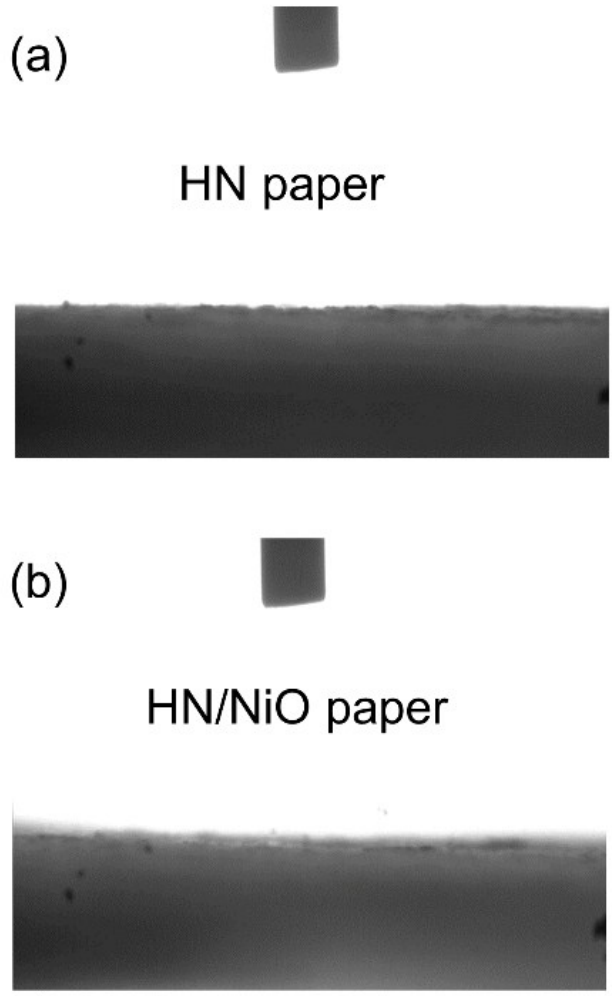

Fig. S8. Water contact angle test of the HN paper (a) and the hydrophilic HN/NiO photothermal paper (b).

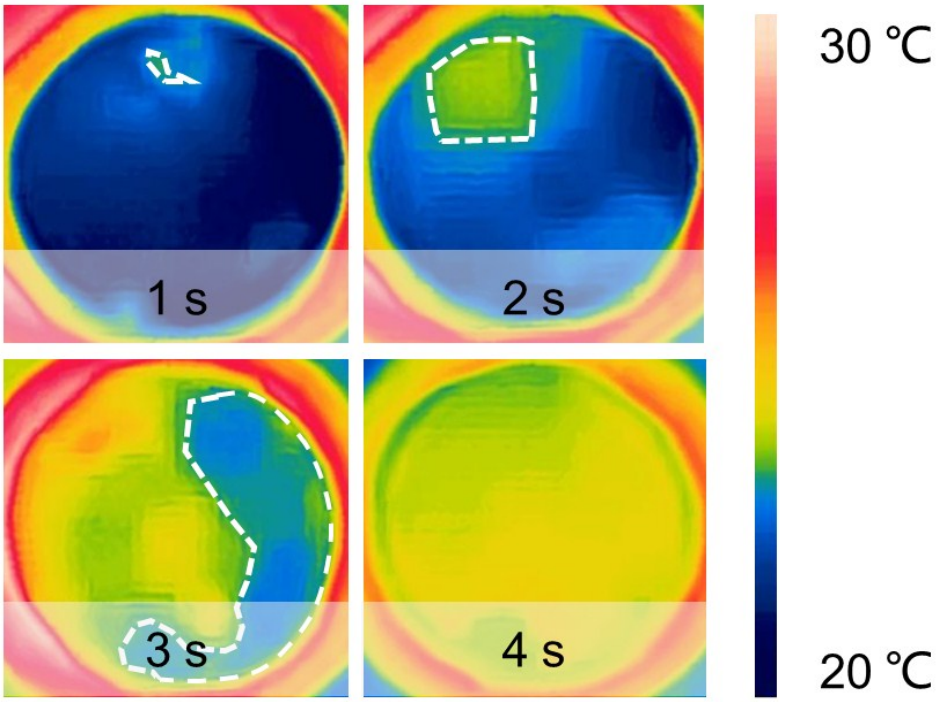

Fig. S9. IR thermal images of the wetting process of the hydrophilic HN/NiO photothermal paper in contact with a wet air-laid paper for different times of 1, 2, 3 and 4 s.

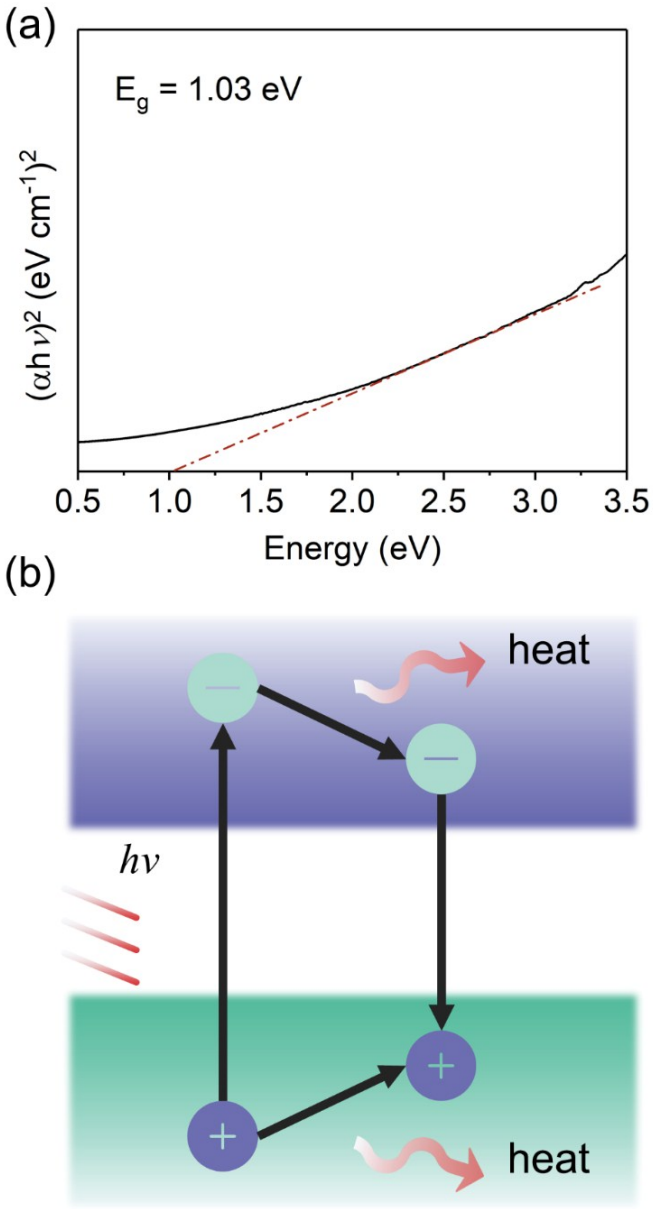

Fig. S10. (a) Plot of $(\alpha h\nu)^2$ versus $h\nu$ of black NiO nanoparticles. (b) Schematic illustration of electron-hole generation and thermalization.

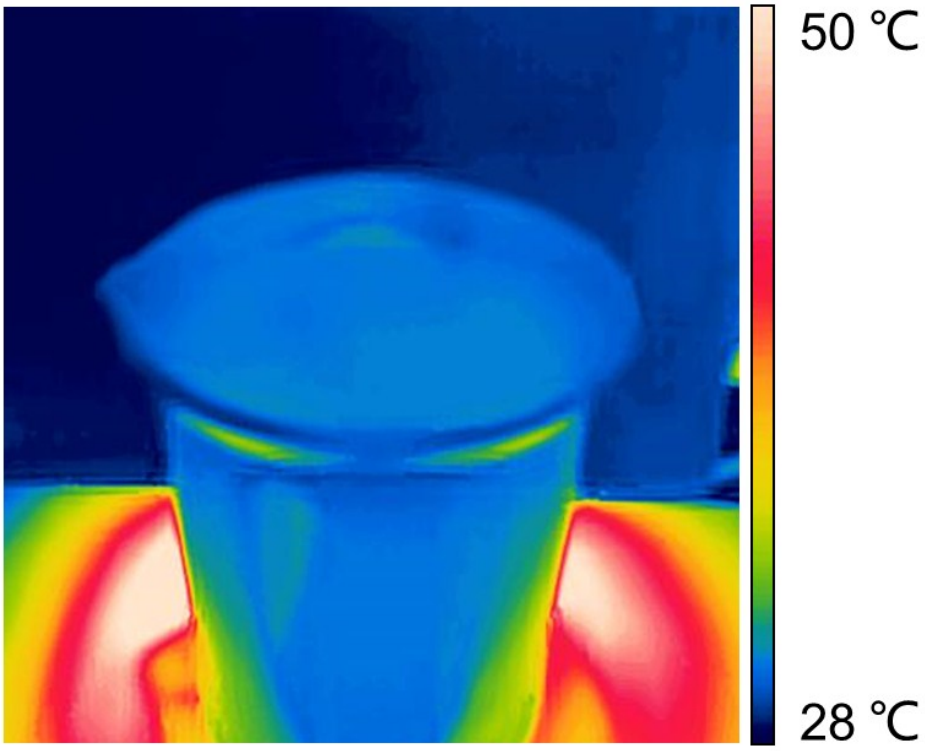

Fig. S11. IR thermal image of the pure water under 1 kW m^{-2} light irradiation for 10 min.

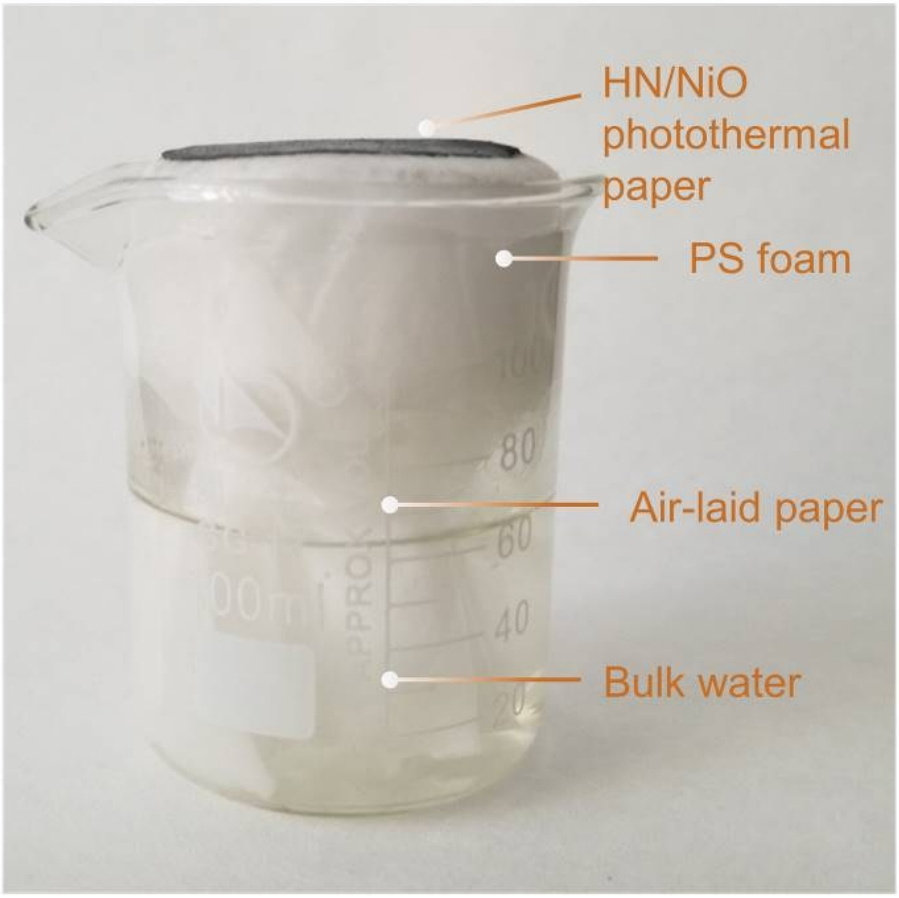

Fig. S12. Digital image of the solar energy-driven water evaporator based on the hydrophilic HN/NiO photothermal paper.

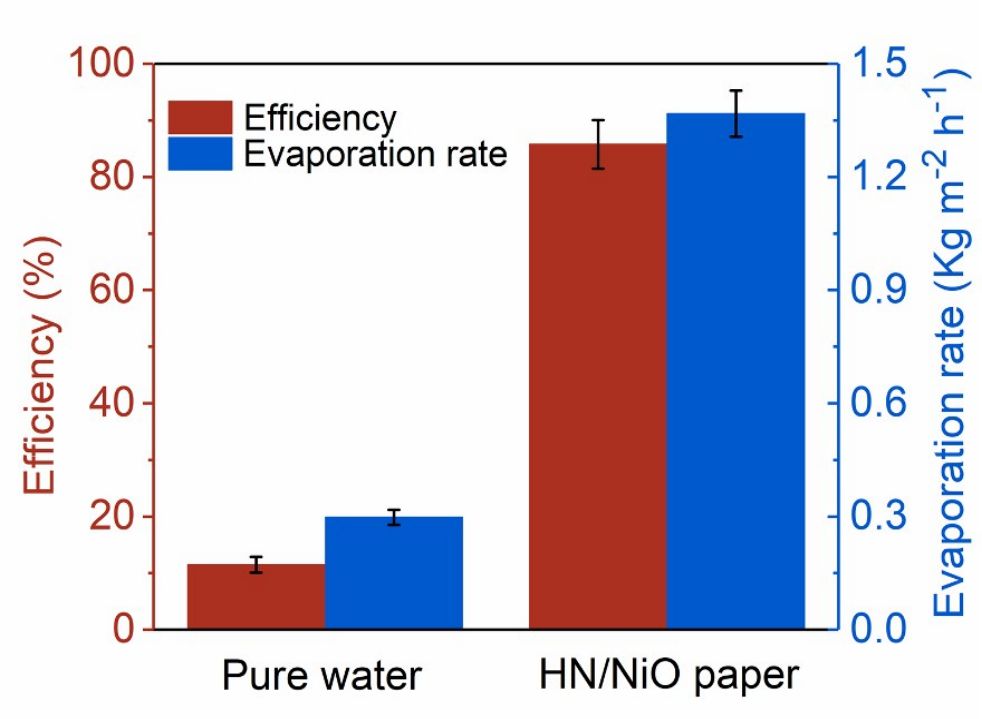

Fig. S13. Comparison of the water evaporation efficiency (red column) and water evaporation rate (blue column) using deionized water without and with the hydrophilic HN/NiO photothermal paper.

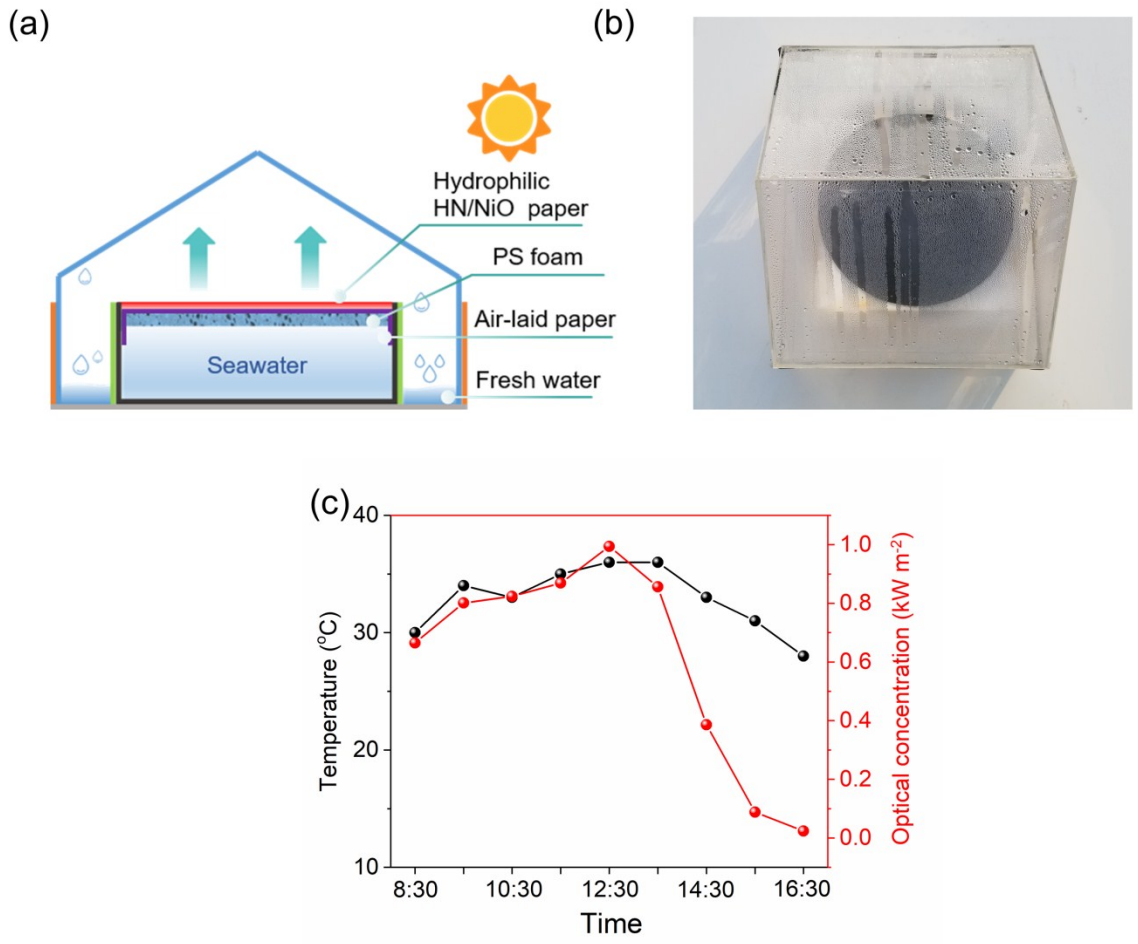

Fig. S14. (a) Schematic illustration and (b) digital image of the outdoor solar energy-driven water evaporator and clean water collector under natural solar light irradiation. (c) Variable solar light intensity and environmental temperature curves from 8:30 a.m. to 4:30 p.m. on May 22, 2019 in Shanghai, China.

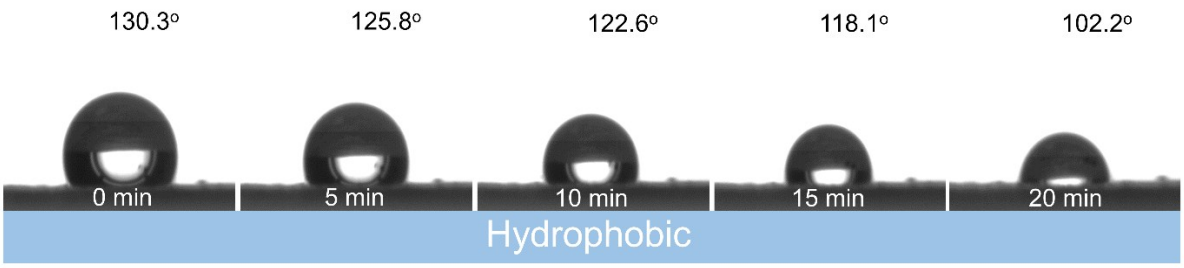

Fig. S15. Water contact angle changing process with time of the hydrophobic HN layer in the Janus HN/NiO photothermal paper.

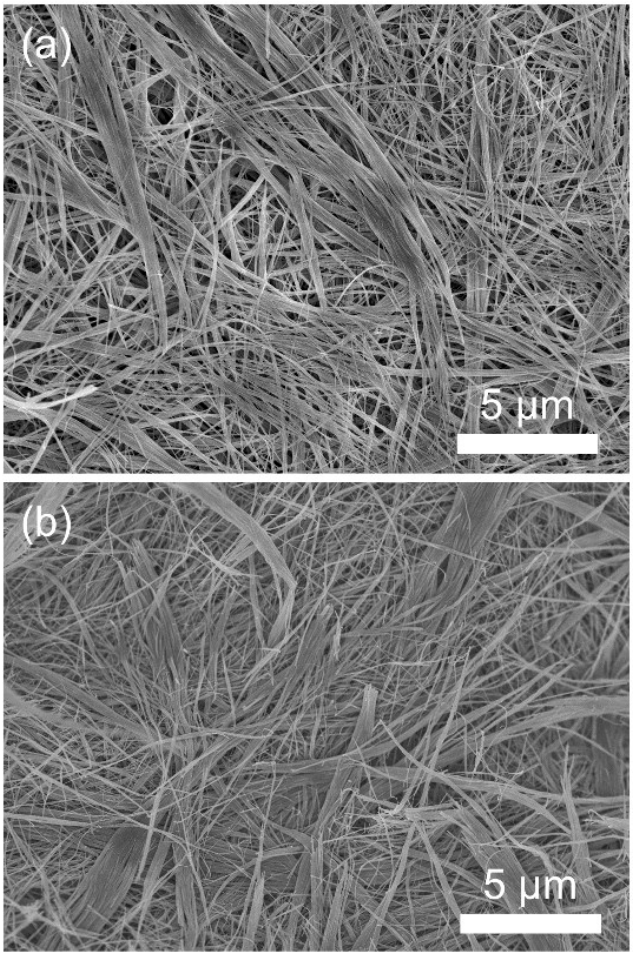

Fig. S16. Surface SEM images of the hydrophilic HN paper (a) and the hydrophobic HN paper (b).

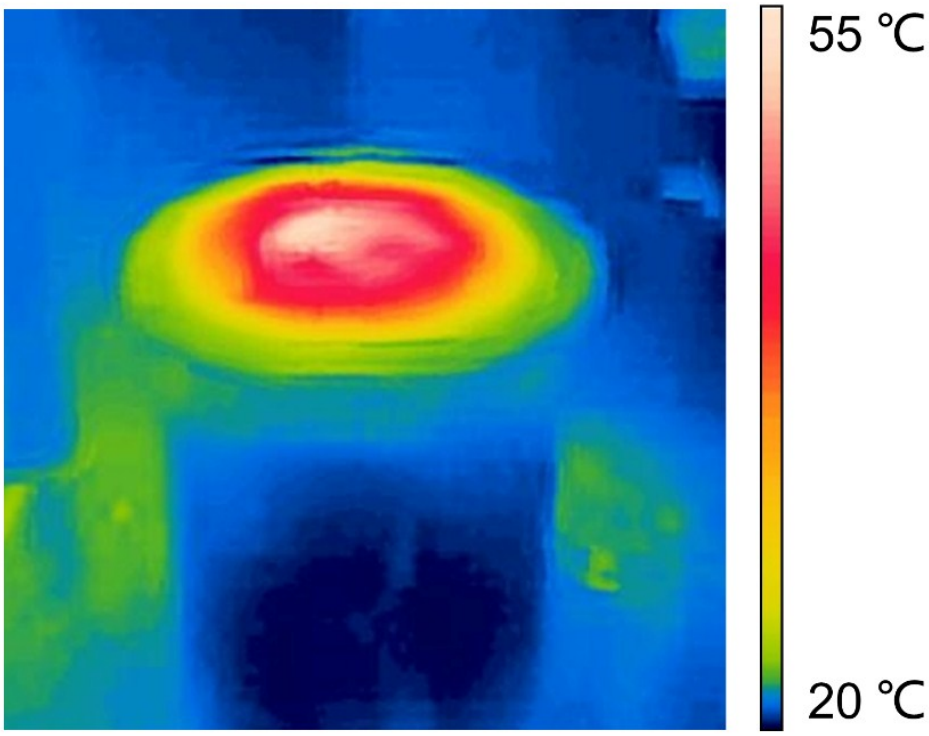

Fig. S17. IR thermal image of the Janus HN/NiO photothermal paper under 1 kW m^{-2} light irradiation for 10 min.

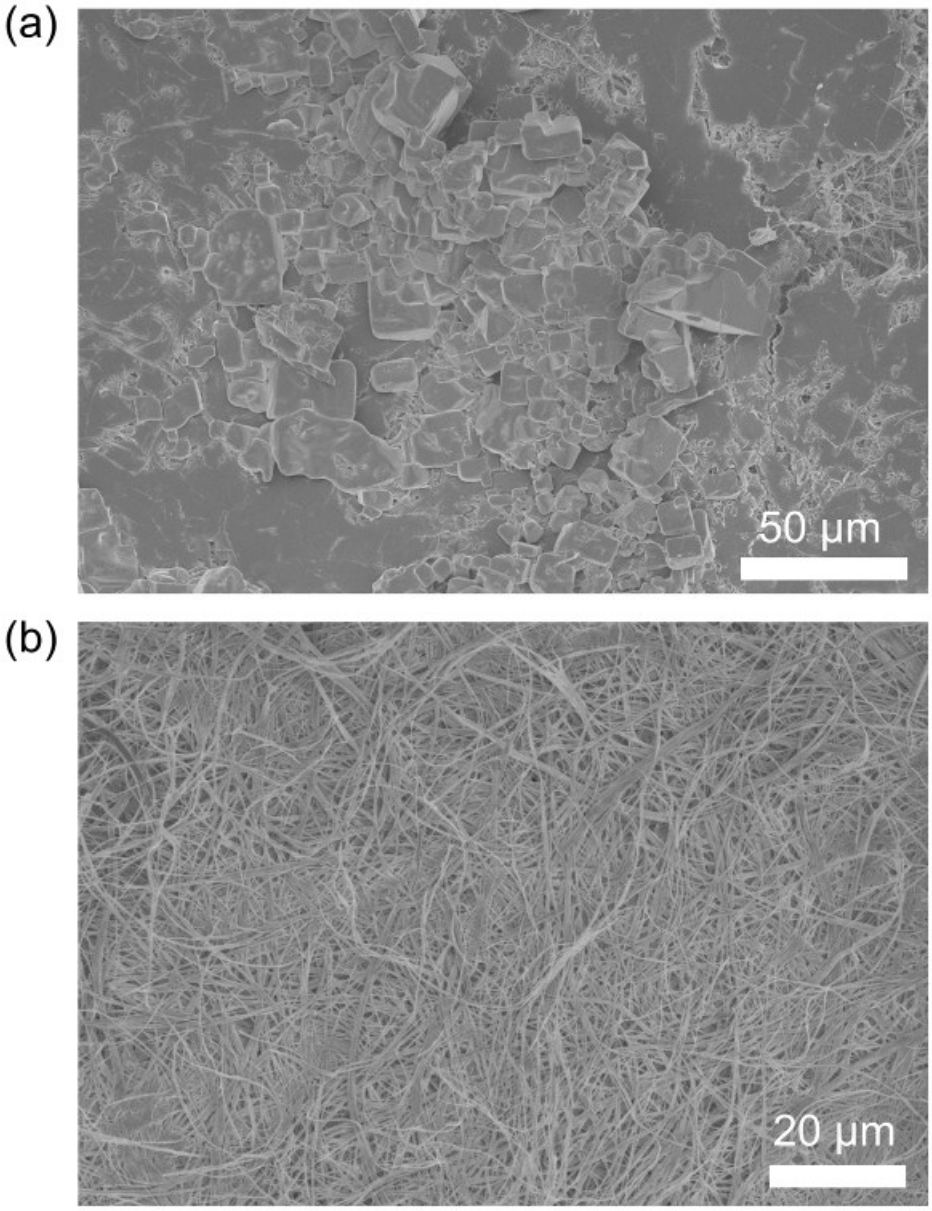

Fig. S18. SEM images of the bottom surface of the hydrophilic HN/NiO photothermal paper (a) and the Janus HN/NiO photothermal paper (b) after 8 h light irradiation at 1 kW m^{-2} using the simulated seawater (3.5 wt.% NaCl).

Table S1. Calculation results of water evaporation efficiencies[a]

C_{op} (kW m^{-2})	$\dot{m}$ (kg m^{-2} h^{-1})[a]	h_{LV} (kJ kg^{-1})[S6]	η (%)
1	1.24	2393.4	85.8
2	2.48	2367.0	86.6
3	3.83	2359.2	89.5

[a] $\dot{m}$ is the water evaporation rate after subtracting the evaporation rate of pure water in darkness.

Table S2. Comparison of solar energy-driven water evaporation performance under 1 kW m^{-2} light irradiation and salt-rejection ability of the Janus HN/NiO photothermal paper with some photothermal materials reported in the literature[b]

Materials	Solar absorption (%)	Evaporation efficiency (%)	Evaporation rate (kg m^{-2} h^{-1})	Salt rejection test	Salt-rejection ability	Reference
Polydopamine coated bacterial nanocellulose	98	78	1.13	No	-	S7
CNT-coated wood membrane	~ 98	65	0.95	No	-	S8
CNT-coated cellulose nanofibril aerogel	97.5	76.3	1.11	No	-	S9
Graphene oxide-based aerogel	~ 92	86.5	1.622	No	-	S10
Vertically aligned graphene membrane	-	86.5	1.62	No	-	S11
Polypyrrole coated stainless steel mesh	-	58	0.92	No	-	S12
Filter paper loaded with black silver	-	95.2	1.38	No	-	S13
Carbonized mushrooms	96	78	1.475	No	-	S14
Black titania	-	70.9	1.13	No	-	S15
Paper-based rGO	~ 90	80.6	1.778	No	-	S16
Surface carbonized wood	>95	74	1.08	No	-	S17

Graphene oxide modified silk fabric	>94	102	1.48	Yes	Washing (Intermittent working)	S18
MXene Ti_3C_2	-	71	1.31	Yes	Hydrophobic effect (Continuous working)	S19
Plasmonic wood	99	67	1.0	Yes	Microchannel (Intermittent working)	S20
Surface carbonized wood	~ 99	57.4	~ 0.8	Yes	Microchannel (Intermittent working)	S21
Hierarchical graphene foam	-	91.4	1.4	Yes	Washing (Intermittent working)	S22
Carbon nanosheet framework	~ 98.3	93	1.48	Yes	Not mentioned	S23
Janus HN/NiO photothermal paper	92.1	83.5	1.33	Yes	Hydrophobic effect (Continuous working)	This work

[b] CNT: carbon nanotube; rGO: reduced graphene oxide.

References

S1. D. Hao, Y. Yang, B. Xu and Z. Cai, *ACS Sustain. Chem. Eng.*, 2018, **6**, 10789-10797.

S2. X. Li, J. Li, J. Lu, N. Xu, C. Chen, X. Min, B. Zhu, H. Li, L. Zhou, S. Zhu, T. Zhang and J. Zhu, *Joule*, 2018, **2**, 1331-1338.

S3. Y. Wang, C. Wang, X. Song, M. Huang, S. K. Megarajan, S. F. Shaukat and H. Jiang, *J. Mater. Chem. A*, 2018, **6**, 9874-9881.

S4. S. Hong, Y. Shi, R. Li, C. Zhang, Y. Jin and P. Wang, *ACS Appl. Mater. Interfaces*, 2018, **10**, 28517-28524.

S5. X. Zhou, F. Zhao, Y. Guo, Y. Zhang and G. Yu, *Energy Environ. Sci.*, 2018, **11**, 1985-1992.

S6. Dortmund Data Bank Software & Separation Technology, DDBST GmbH, Oldenburg 2016.

S7. Q. Jiang, H. Gholami Derami, D. Ghim, S. Cao, Y.S. Jun and S. Singamaneni, *J. Mater. Chem. A*, 2017, **5**, 18397-18402.

S8. C. Chen, Y. Li, J. Song, Z. Yang, Y. Kuang, E. Hitz, C. Jia, A. Gong, F. Jiang, J.Y. Zhu, B. Yang, J. Xie and L. Hu, *Adv. Mater.,* 2017, **29**, 1701756.

S9. F. Jiang, H. Liu, Y. Li, Y. Kuang, X. Xu, C. Chen, H. Huang, C. Jia, X. Zhao, E. Hitz, Y. Zhou, R. Yang, L. Cui and L. Hu, *ACS Appl. Mater. Interfaces*, 2018, **10**, 1104-1112.

S10. X. Hu, W. Xu, L. Zhou, Y. Tan, Y. Wang, S. Zhu and J. Zhu, *Adv. Mater.*, 2017, **29**, 1604031.

S11. P. Zhang, J. Li, L. Lv, Y. Zhao and L. Qu, *ACS Nano*, 2017, **11**, 5087-5093.

S12. L. Zhang, B. Tang, J. Wu, R. Li and P. Wang, *Adv. Mater.*, 2015, **27**, 4889-4894.

S13. J. Chen, J. Feng, Z. Li, P. Xu, X. Wang, W. Yin, M. Wang, X. Ge, Y. Yin, *Nano Lett.*, 2018, **19**, 400-407.

S14. N. Xu, X. Hu, W. Xu, X. Li, L. Zhou, S. Zhu and J. Zhu, *Adv. Mater.*, 2017, **29**, 1606762.

S15. G. Zhu, J. Xu, W. Zhao and F. Huang, *ACS Appl. Mater. Interfaces*, 2016, **8**, 31716-31721.

S16. Z. Wang, Q. Ye, X. Liang, J. Xu, C. Chang, C. Song, W. Shang, J. Wu, P. Tao and T.

Deng, *J. Mater. Chem. A*, 2017, **5**, 16359-16368.

S17. H. Liu, C. Chen, G. Chen, Y. Kuang, X. Zhao, J. Song, C. Jia, X. Xu, E. Hitz, H. Xie, S. Wang, F. Jiang, T. Li, Y. Li, A. Gong, R. Yang, S. Das and L. Hu, *Adv. Energy Mater.*, 2018, **8**, 1701616.

S18. Q. Zhang, X. Xiao, G. Wang, X. Ming, X. Liu, H. Wang, H. Yang, W. Xu and X. Wang, *J. Mater. Chem. A*, 2018, **6**, 17212-17219.

S19. J. Zhao, Y. Yang, C. Yang, Y. Tian, Y. Han, J. Liu, X. Yin and W. Que, *J. Mater. Chem. A*, 2018, **6**, 16196-16204.

S20. M. Zhu, Y. Li, F. Chen, X. Zhu, J. Dai, Y. Li, Z. Yang, X. Yan, J. Song, Y. Wang, E. Hitz, W. Luo, M. Lu, B. Yang and L. Hu, *Adv. Energy Mater.*, 2018, **8**, 1701028.

S21. M. Zhu, Y. Li, G. Chen, F. Jiang, Z. Yang, X. Luo, Y. Wang, S.D. Lacey, J. Dai, C. Wang, C. Jia, J. Wan, Y. Yao, A. Gong, B. Yang, Z. Yu, S. Das and L. Hu, *Adv. Mater.*, 2017, **29**, 1704107.

S22. H. Ren, M. Tang, B. Guan, K. Wang, J. Yang, F. Wang, M. Wang, J. Shan, Z. Chen, D. Wei, H. Peng and Z. Liu, *Adv. Mater.*, 2017, **29**, 702590.

S23. L. Sun, J. Liu, Y. Zhao, J. Xu and Y. Li, *Carbon*, 2019, **145**, 52-358.